Tellus SERIES B CHEMICAL AND PHYSICAL METEOROLOGY
PUBLISHED BY THE INTERNATIONAL METEOROLOGICAL INSTITUTE IN STOCKHOLM

Tellus (2011), 63B, 287–301
Printed in Singapore. All rights reserved

© 2011 NZ National Institute of Water & Atmospheric Research
Tellus B © 2011 John Wiley & Sons A/S

TELLUS

Seasonal inter-relationships in atmospheric methane and companion δ^{13}C values: effects of sinks and sources

By K. R. LASSEY[1]*, W. ALLAN[2] and S. E. MIKALOFF FLETCHER[1], [1]*NIWA, PO Box 14-901, Kilbirnie, Wellington 6241, New Zealand;* [2]*Allan Planning and Research Ltd., 26 Patrick St, Petone 5012, New Zealand*

(Manuscript received 14 September 2010; in final form 29 March 2011)

ABSTRACT

Recent developments in applying carbon-isotope information to better understand regional and global methane budgets infer a strong role by a highly fractionating seasonal sink such as atomic chlorine. Specifically, OH as the predominant seasonal sink cannot account for the 'phase ellipses' based on observed seasonal cycles of methane mixing ratio and isotope ratio, δ^{13}C. Although a strong role by atomic chlorine is inferred empirically, open questions remain about the interplay between sources and sinks in determining the properties of phase ellipses. This paper employs a simple didactic model of the seasonal cycling of atmospheric methane to understand such interplay. We demonstrate that a single seasonal sink and seasonal source act together to imprint anti-phase seasonalities on atmospheric methane and δ^{13}C, which lead to phase ellipses that collapse onto a straight line with slope characteristic of that sink. This explains empirical findings of these anti-phase relationships in three-dimensional modelling studies. We also demonstrate that multiple seasonal sinks acting with a seasonal source can yield surprising properties for the phase ellipse that not only explain some features of phase ellipses reported in modelling studies but also have the potential to explain marked inter-annual variation in phase ellipses based on observation.

1. Introduction

Methane (CH_4) is the second most important anthropogenic greenhouse gas after CO_2 with a much higher global warming potential (Forster et al., 2007). It plays a significant role in ozone chemistry, which determines the oxidizing capacity of the atmosphere (Denman et al., 2007). Despite its first-order importance to climate change and atmospheric chemistry, regional and global CH_4 budgets are still highly uncertain. Furthermore, atmospheric CH_4 observations reveal inter-annual variability and trends in the growth rate over the last two decades that are still poorly understood (Dlugokencky et al., 2003; Rigby et al., 2008; Dlugokencky et al., 2009; Lassey et al., 2010).

Atmospheric observations of $^{13}C/^{12}C$ isotopic ratios in CH_4 contain information about influential source and sink processes that are a result of characteristic isotopic signatures of the CH_4 sources and isotopic fractionations of the sinks. Measurements of co-located CH_4 mixing ratio ([CH_4]) and isotopic ratio (δ^{13}C, defined later) in the atmosphere have been widely used to improve estimates of CH_4 sources and sinks (e.g. Fung et al., 1991; Mikaloff Fletcher et al., 2004a,b), validate models (e.g. Bergamaschi et al., 2001) and interpret drivers of variability of atmospheric CH_4 on synoptic, seasonal and inter-annual timescales (e.g. Francey et al., 1999; Tarasova et al., 2007). In addition, detailed analysis of inter-relationships between the seasonal cycles in [CH_4] and its δ^{13}C further constrain isotopic signatures and fractionations over large spatial regions (e.g. Lowe et al., 1999; Bergamaschi et al., 2000; Allan et al., 2001a,b; Platt et al., 2004; Allan et al., 2005, 2007).

As per convention, isotope ratios $^{13}C/^{12}C$ are reported numerically in 'per mil' (‰) notation δ^{13}C defined by

$$\delta^{13}C = (R_A/R_{std} - 1) \times 1000. \quad (1)$$

Here, R_A is the $^{13}C/^{12}C$ molar ratio in the methane sample and R_{std} is the corresponding ratio in the carbon isotope standard, Vienna Peedee belemnite (VPDB). The factor 1000 in eq. (1) is omitted from mathematical expressions, so that a δ^{13}C value of, say, −47‰ is treated algebraically as −0.047.

The 'fractionation factor' for a specific sink can be defined as

$$\alpha \equiv 1 + \varepsilon = k_{13}/k_{12}, \quad (2)$$

where k_n is the removal rate of $^nCH_4$ by that sink. We refer to ε, expressed also in ‰, as the kinetic isotope effect (KIE) for the particular sink. Because $k_{12} > k_{13}$, ε is always negative with this particular definition of α.

---

*Corresponding author.
e-mail: k.lassey@niwa.co.nz
DOI: 10.1111/j.1600-0889.2011.00535.x

In the Northern Hemisphere (NH) and the tropics, the seasonal cycles of CH_4 and $\delta^{13}C$ display strong spatial and temporal variabilities that are driven primarily by seasonal sources that are more depleted in ^{13}C than atmospheric CH_4, compounded by more irregular ^{13}C-enriched emissions during large-scale burning of biomass (e.g. Dlugokencky et al., 1994; Miller et al., 2002; Tyler et al., 2007). Contrastingly, seasonal cycles of CH_4 and $\delta^{13}C$ in the extra tropical Southern Hemisphere (ETSH) show much greater spatial homogeneity (Dlugokencky et al., 1994). Time series of CH_4 and $\delta^{13}C$ from two baseline observing stations in the ETSH and regular observations from Pacific Ocean ship tracks indicate that the region south of the South Pacific Convergence Zone (20–30°S) is well mixed, and their respective seasonal cycles are largely determined by in situ oxidation of CH_4 (Lassey et al., 1993; Lowe et al., 1999).

Over the last decade, a series of studies (e.g. Allan et al., 2001b; Platt et al., 2004; Allan et al., 2005, 2007) has revealed how co-located observations of the seasonal cycles of CH_4 and $\delta^{13}C$ in CH_4 at stations in the ETSH could constrain the KIE of CH_4 sinks. Allan et al. (2001b) constructed 'phase diagrams' by plotting intra-annual variations in $\delta^{13}C$ against the corresponding variations in $[CH_4]$, an approach that had proven fruitful in CO_2 studies (e.g. Francey, 1985; Keeling et al., 1989). In the ETSH, these phase diagrams displayed a characteristic elliptical shape oriented along a 'KIE line' (Section 2).

The dominant sink of atmospheric CH_4 is oxidation by the OH radical. Based on laboratory studies, the KIE for this reaction has magnitude 3.9–5.4‰ (Cantrell et al., 1990; Saueressig et al., 2001), which is too small to explain the slopes of the KIE lines derived from observations at Baring Head, New Zealand, and Arrival Heights, Antarctica. Furthermore, the 'apparent KIE' deduced from those slopes shows marked inter-annual variability (Allan et al., 2005). Allan et al. (2001a,b) hypothesized that the large apparent KIE may be due to an oxidative role by atomic chlorine in the marine boundary layer (MBL). Atomic chlorine is distinguished by fractionating CH_4 very strongly, markedly influencing $\delta^{13}C$ in CH_4 (e.g. Saueressig et al., 1995; Gupta et al., 1996), even though its global strength is thought to be relatively small and commonly not considered in CH_4 budgets.

With few measurements available of Cl in the MBL, Platt et al. (2004) and Allan et al. (2005, 2007) constructed spatial and seasonal Cl patterns that are consistent with available measurements and with likely production mechanisms, and that can account for CH_4 data at Baring Head and Arrival Heights, including the apparent KIE. Those studies suggested that atomic Cl could remove 13–37 Tg CH_4 per year globally. The possibility that the strengths of seasonal sources and their inter-annual variabilities could account for the apparent KIE and its variability was discounted in a modelling study which, by doubling then zeroing individual source strengths, demonstrated that the apparent KIE in the ETSH is insensitive to such large perturbations (Allan et al., 2010).

Although phase ellipses provide an intriguing tool for interpreting CH_4 data and model output, work published to date is empirical in nature, lacking a deeper mechanistic understanding of the interplay between the seasonal cycles of CH_4 and $\delta^{13}C$. The goal of this paper is to examine the roles of seasonal sources and sinks in determining the properties of phase ellipses, including potential causes of variability in those properties.

First, we briefly review phase diagrams and open questions about the processes governing them that are raised by Allan et al. (2001b). We then develop a simple and highly idealized algebraic model to describe the seasonality in the CH_4 budget and explore the origins of phase diagrams. We apply the model numerically to explore two didactic cases: a single seasonal source with a single seasonal sink, and a single seasonal source with dual seasonal sinks. Finally, we discuss the implications of this work for the previous studies of Allan et al. (2001a,b; 2005; 2007; 2010), and the future potential of the phase diagram approach.

2. Phase diagrams and the KIE line

Each phase diagram is a plot through an annual cycle of $\Delta\delta$, the departure of atmospheric $\delta^{13}C$ from its annual mean, $\bar{\delta}$, against $\Delta C/\bar{C}$, the corresponding relative departure of atmospheric CH_4 mixing ratio or burden from its mean, $\bar{C}$. Each of $\Delta\delta$ and $\Delta C/\bar{C}$ may be based on co-located observation, or be model output (most instructively, for a single source type), and may be detrended where the trend is comparable to seasonal variation.

Phase diagrams for ETSH sites derived using the TM2 model (Heimann, 1995) with OH as the sole seasonal sink are nearly elliptical in shape and denoted 'phase ellipses' (Allan et al., 2001b, Fig. 1). The following two robust features of phase ellipses were reported by Allan et al. (2001b): (1) the ellipse is both tilted and elongated (i.e. has high eccentricity, with the breadth exaggerated by the implicit factor of 1000 in the ‰ units) and (2) the slope of the ellipse major axis (elliptical 'tilt') is proportional to the KIE value for the OH sink and given by the 'KIE line':

$$\Delta\delta = \{\varepsilon(1+\bar{\delta})\}(\Delta C/\bar{C}). \tag{3}$$

The robustness of these features was checked by repetitively running TM2 with varied sink details, including different KIE values.

Allan et al. demonstrated that for any individual source component, whether deemed aseasonal (such as livestock) or highly seasonal (such as biomass burning), a TM2-derived phase ellipse for any location in either hemisphere collapses onto a straight line given by the KIE line (3) (Allan et al., 2001b, Figs 6 and 7). We illustrate this even more strongly in Fig. 1, where at latitude 3.9° and longitude 180° the TM2-derived mixing ratio and $\delta^{13}C$ time-series are highly variable with little evidence of a smooth seasonal cycle. Even so, the phase ellipse shown in the bottom panel of Fig. 1 is indistinguishable from a straight line that is very close to the KIE line deduced from (3). Thus, $\Delta\delta$ and ΔC

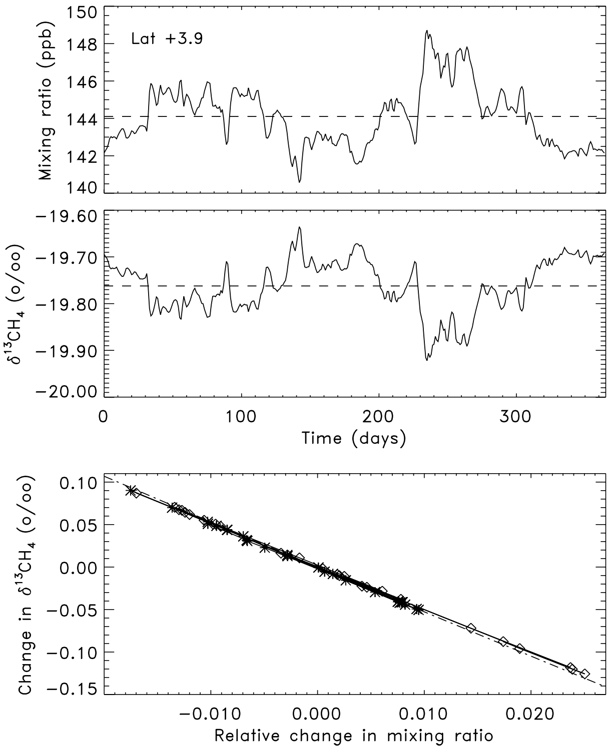

Fig. 1. The upper two panels show seasonal pattern of the imprint of biomass burning (45 Tg(CH_4) yr^{-1} globally) on atmospheric CH_4 mixing ratio and companion $\delta^{13}C$ in the oceanic cell with central latitude 3.9°N and longitude 180°, as simulated by Allan et al. (2001b) using the TM2 atmospheric tracer transport model (not shown in that paper). Dashed lines show annual mean values. The lowest panel shows the corresponding phase diagram with 2-weekly averaged values, marked with asterisks January to June and diamonds July to December. The dash–dot line is the KIE line of eq. (3) corresponding to a single OH sink with $\varepsilon_{OH} = -5.4‰$ as used in the simulation.

are highly anti-correlated for an individual source component. This feature was unexplained.

Rayleigh distillation provides a description of isotopic enrichment that occurs in a system with an irreversible sink process (e.g. Rahn et al., 1998; Scott et al., 2004). In our notation, the Rayleigh distillation equation is

$$\Delta\delta = \{(1 + \Delta C/\bar{C})^{\varepsilon} - 1\}(1 + \bar{\delta}). \tag{4}$$

In the range of $\Delta C/\bar{C}$ shown in Fig. 1, (3) is an excellent approximation to (4). Thus, (3) can be thought of as describing Rayleigh distillation during periods of sink dominance (left to right along the KIE line), followed by 'inverse Rayleigh distillation' during periods of source dominance during which the CH_4 removed is replenished to recover the initial state.

3. Model specification

We pose the following question. If atmospheric CH_4 in a 'coherent' region of the atmosphere (i.e. a region largely devoid of spatial gradients) is driven by source(s) and sink(s) whose strengths have a regular seasonal pattern but no trend, what are the relationships between those seasonal patterns and the seasonalities that result in atmospheric CH_4 and in its $\delta^{13}C$ signature? In this context, we consider 'seasonalities' to embrace both seasonal amplitude and phase. The coherent region could be as small as the smallest-resolved volume in a three-dimensional (3-D) model or as large as the ETSH or even the full SH.

The seasonal relationships are illustrated using a 'sinusoidal model': a single well-mixed box characterizes the coherent atmosphere, in which the CH_4 and $^{13}CH_4$ burdens (or mixing ratios) are driven by a seasonally varying source strength and a seasonally varying sink strength that are idealized as sinusoidal with annual period. Mass balance of total CH_4 in the box requires that

$$\frac{\partial C(t)}{\partial t} = S(t) - \lambda(t)C(t), \tag{5}$$

where $S(t)$ is the CH_4 source (Tg yr^{-1}) to the atmospheric box of CH_4 burden $C(t)$ (Tg) from which CH_4 is removed at a fractional rate of $\lambda(t)$ per annum (yr^{-1}) by first-order sinks. An analogous equation applies for $^{13}CH_4$. The CH_4 burden is in a 'cyclo-stationary state', a steady-state perturbed by recurring seasonality driven by seasonal source and sink that the time (t) dependence reflects. The source $S(t)$ includes both surface sources and transport-mediated fluxes to and from adjoining boxes. This is analogous to the approach of Lassey et al. (1993) who considered a 'composite source' to the SH atmosphere comprising all indigenous SH sources together with a 'spillover source' due to net exchange with the atmosphere to the north.

Our sinusoidal model isolates a single 'source type', $S(t)$, characterized by a fixed isotope signature $\delta^{13}C$, denoted δ_S. This can be thought of as a component of a disaggregated source. A coarse disaggregation might be biogenic, fossil, and pyrogenic methane, each with a characteristic $\delta^{13}C$, or, in a finer disaggregation, $S(t)$ could represent all CH_4 emissions from, for example rice agriculture with its $\delta^{13}C$ signature. The imprint of $S(t)$ on the model atmosphere in conjunction with sink $\lambda(t)$ with fixed KIE ε is the burden, $C(t)$ and companion $\delta^{13}C$ value, denoted $\delta_C(t)$. In aggregating over component source types, the combined burden is the aggregate of component burdens, whereas the combined $\delta^{13}C$ value is, to first order, the mean of individual $\delta_C(t)$ weighted by respective burdens, as per summing source-weighted $\delta^{13}C$ to give $\delta^{13}C$ in the global source (e.g. Lassey et al., 2000, Table 1). Such aggregation of source types is an approach commonly adopted in modelling studies (e.g. Fung et al., 1991; Allan et al., 2001b).

In developing first the case of a single seasonal sink in concert with a single seasonal source (Section 4), and then a dual seasonal sink and single seasonal source (Section 5), we relegate to appendices mathematical detail that might otherwise distract the logical model development. Sinusoidal sources and sinks are

Table 1. Parameter values used to illustrate the sinusoidal model, approximately representative of a hemispheric-mean sink together with a nominal source

Parameter	Single-sink case	Dual-sink case
Source		
S_0 (Tg yr^{-1})	100	105
S_1 (Tg yr^{-1})	20	21
θ_S (rad)	$\pi/12$	$\pi/12$
δ_S (‰)	−60	−60
Primary sink		
λ_{10} (yr^{-1})	0.11	0.11
λ_{11} (yr^{-1})	0.04	0.04
ε_1 (‰)	−4.0	−4.0
Secondary sink		
λ_{20} (yr^{-1})		$0.05\lambda_{10}$
λ_{21} (yr^{-1})		$0.9\lambda_{20}$
ε_2 (‰)		−62
Derived sinusoidal output		
C_0 (Tg)	909.09	909.09
C_1 (Tg)	2.84	3.39
θ_C (rad)	1.276	1.276
δ_0 (‰)	−56.225	−53.601
δ_1 (‰)	0.012	0.048
θ_δ (rad)	−1.866	−1.698
$\bar{\varepsilon}$ (‰)		−6.76
$\tilde{\varepsilon}$ (‰)		−10.39

illustrated using values approximately representative of the SH mean (Table 1).

4. Single seasonal sink

Consider first the relationships imposed by mass balance of total methane, followed by relationships between isotope ratios developed through mass balance of $^{13}CH_4$. For simplicity and with minimal error, the ratios $^{13}C/^{12}C$ and $^{13}C/(^{12}C+^{13}C)$ are not distinguished. The mathematical framework is adapted in part from Lassey et al. (1993).

4.1. Seasonality of total methane

The model atmosphere of (5) is driven by source and sink of the form

$$S(t) = S_0 + S_1 \cos(\omega t + \theta_S)$$

$$\lambda(t) = \lambda_0 + \lambda_1 \cos(\omega t) \tag{6}$$

in which $\omega = 2\pi$ yr^{-1}, S_0 and λ_0 are annual mean values, and S_1 and λ_1 are non-negative seasonal amplitudes that cannot exceed the respective annual means. The absence of an explicit phase in $\lambda(t)$ merely defines 'time zero' without loss of generality, so that θ_S is the phase angle between source and sink. Fig. 2(a) illustrates the functional forms (6).

The analytical solution for $C(t)$ is not tractable. However, it is possible to isolate the leading harmonic for $C(t)$ of the form

$$C(t) = C_0 + C_1 \cos(\omega t + \theta_C) \tag{7}$$

and solve for its parameters, C_0, C_1 (non-negative) and θ_C. This is achieved by back-substituting (6) and (7) into (5) and treating the result as an identity in time, with second and higher harmonics ignored (Appendix A). Separating time-independent components from the identity yields:

$$S_0 - \lambda_0 C_0 = \frac{1}{2}\lambda_1 C_1 \cos(\theta_C). \tag{8}$$

Separating first harmonic components yield:

$$C_1\omega \cos(\theta_C) = S_1 \sin(\theta_S)$$

$$C_1\omega \sin(\theta_C) = \lambda_1 C_0 - S_1 \cos(\theta_S). \tag{9}$$

The former of eqs (9) enables the right-hand side (RHS) of (8) to be expressed in terms of its source–sink drivers:

$$S_0 - \lambda_0 C_0 = \frac{1}{2}\frac{\lambda_1}{\omega} S_1 \sin(\theta_S) \tag{10}$$

with $\lambda_1/\omega < \lambda_0/\omega \approx 0.02$ for CH_4, as long as S_1/S_0 is sufficiently small the RHS of (10) can be ignored to yield

$$S_0 = \lambda_0 C_0. \tag{11}$$

Equation (11) is the customary relationship for a steady source and sink in equilibrium with an atmospheric burden. It is usually taken also to relate the means of seasonally varying entities. However, (10) indicates that a correction should in principle apply unless either the source or sink is aseasonal, or they are in phase or antiphase ($\theta_S = 0$ or π). Furthermore, numerical experimentation reveals that when (11) is used to estimate C_0, the error made through ignoring RHS of (10) may be of comparable magnitude to the amplitude C_1 (one can show that this error has upper bound $(1/2)(S_1/S_0)C_1$).

Equations (9) and (11) can be thought of as providing solutions, C_0, C_1, θ_C, for atmospheric seasonality in CH_4 (see Appendix A for explicit expression). For an aseasonal source, $S_1 = 0$, atmospheric seasonality is necessarily fully sink driven with parameters

$$\theta_C = \pi/2,\ C_1 = (\lambda_1/\omega)C_0. \tag{12}$$

Conversely, for a dominant source seasonality, $S_1/S_0 \gg \lambda_1/\lambda_0$ (which could apply in tropical regions with emissions driven by seasonal hydrological cycles), then

$$\theta_C \to \theta_S - \pi/2,\ C_1 \to S_1/\omega. \tag{13}$$

In between these extremes, relative amplitude C_1/C_0 is never less than $(\lambda_1/\omega)|\sin(\theta_S)|$. (This lower bound leads to the upper bound on the 'error in C_0' mentioned following eq. 11). Nonetheless, eqs (9) and (11) confirm that atmospheric $C(t)$ will be aseasonal ($C_1 = 0$) in the event that source and sink are both in phase ($\theta_S = 0$) and have identical relative amplitudes

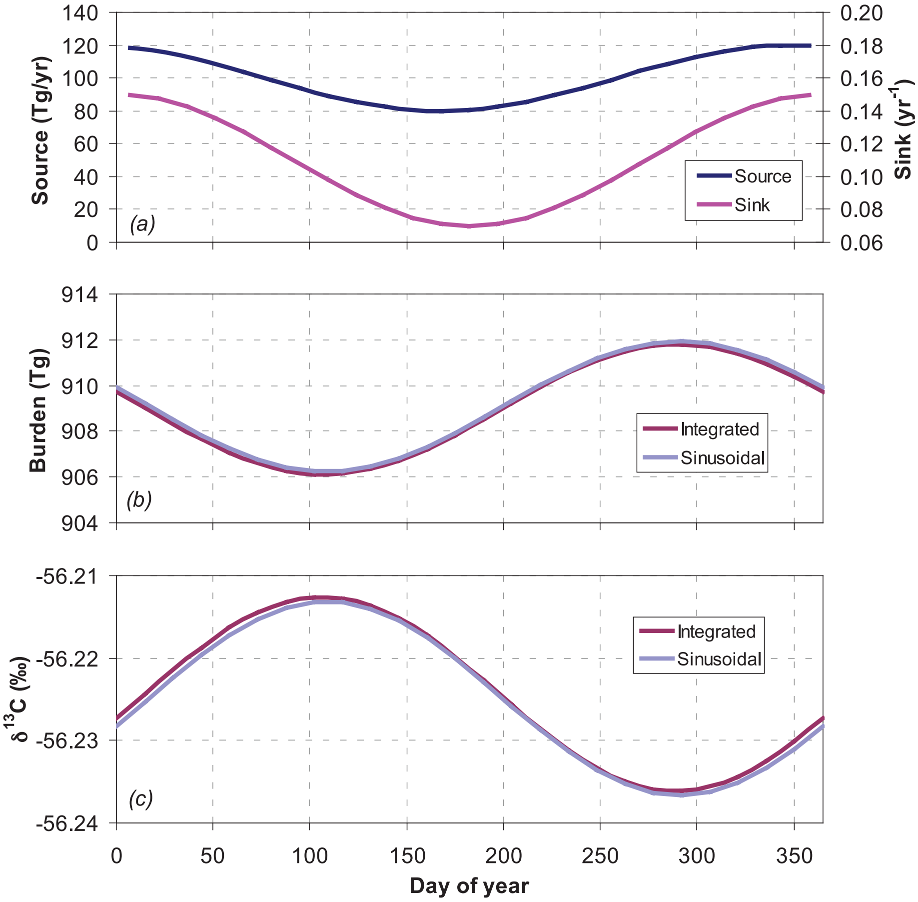

Fig. 2. Simulations with the ‘sinusoidal model’ with a single source and single sink, using the parameters of Table 1. Panel (a) shows the driving source and sink of eq. (6). Panels (b) and (c) show the imprints of that combination on the atmospheric burden and on its δ^{13}C, respectively. Each of the lower two panels reports both the numerical integration of the mass balance equations (‘Integrated’: the last year of 150-yr spin-up of eqs (5) and (14) with 14-day time step), and the sinusoidal approximation (‘Sinusoidal’) of eqs (7) and (15).

($S_1/S_0 = \lambda_1/\lambda_0$). Under those circumstances, source and sink seasonalities completely counteract each other.

Solutions for C_0, C_1, θ_C corresponding to the source–sink parameters of Table 1 are shown also in Table 1.

Fig. 2(b) illustrates $C(t)$. In that figure, $C(t)$ is computed by numerically solving (5) and (6) (with 150-year spin-up time to remove a dependence on initial state), yielding a seasonality that is barely distinguishable from the sinusoid (7) with (9) and (11), also shown in Fig. 2(b).

4.2. Seasonality of $\delta^{13}C$

The analogue of (5) for ^{13}CH$_4$ can be written as

$$\frac{\partial}{\partial t}[(1+\delta_C(t))C(t)] = (1+\delta_S)S(t) - \alpha\lambda(t)(1+\delta_C(t))C(t). \tag{14}$$

In this equation, ^{12}CH$_4$ is not distinguished from CH$_4$ (and as a result the isotope ratio in the international VPDB standard, R_{std}, does not enter the equation); $\alpha = 1 + \varepsilon$ is the isotope fractionation factor of eq. (2) for the particular sink.

Just as in the ‘total methane’ case, the solution to (14) with (6) is made tractable by isolating the lead harmonic analogously to (7):

$$\delta_C(t) = \delta_0 + \delta_1 \cos(\omega t + \theta_\delta) \tag{15}$$

with δ_1 non-negative.

Through back-substitution into the mass-balance eqs (5) and (14), counterparts of (8)–(11) can be developed (Appendix B), with the resulting counterpart of (8):

$$(\mu - \nu)S_0 = \frac{1}{2}\alpha\lambda_1\delta_1 C_0 \cos(\theta_\delta). \tag{16}$$

Here μ and ν emerge as natural abbreviations (both negative):

$$\mu = \delta_S - \delta_0, \quad \nu = \varepsilon(1 + \delta_0). \tag{17}$$

As with (8), the RHS of (16) would normally have very much smaller magnitude than μS_0 and νS_0 (but may still be comparable to the amplitude $|\mu|S_1$), leading to the more common ‘isotope mass balance' constraint

$$\mu = \nu \quad \text{or} \quad \delta_0 = (\delta_S - \varepsilon)/\alpha. \tag{18}$$

The latter is often applied in an approximate form, $\delta_0 \approx \delta_S - \varepsilon$, which views sink fractionation as imposing an isotope 'shift' on δ_S to yield an atmospheric δ^{13}C of δ_0. Such a view can obscure recognition of (18) as the more accurate expression (Lassey et al., 2000).

The isotope counterpart of (9) is

$$\delta_1 \omega C_0 \cos(\theta_\delta) = \mu S_1 \sin(\theta_S)$$

$$\delta_1 \omega C_0 \sin(\theta_\delta) = \nu \lambda_1 C_0 - \mu S_1 \cos(\theta_S). \tag{19}$$

On applying (18) to (19) it is immediately clear that eqs (9) and (19) are proportional, with the corollary (recalling that μ, $\nu < 0$):

$$\delta_1/|\nu| = C_1/C_0, \quad \theta_\delta = \theta_C \pm \pi. \tag{20}$$

The first equality in (20) indicates that the amplitude δ_1 is as small when compared to $|\nu|$ as C_1 is when compared to C_0. Thus, $|\nu|$ plays the role of a scale against which amplitude δ_1 can be compared, noting that δ^{13}C values themselves have an artificial zero governed by the isotope standard. The second equality in (20) reports the important finding that $C(t)$ and $\delta_C(t)$ are always in anti-phase for a single source type and a single seasonal sink.

This robust anti-phase relationship was observed in numerical modelling studies by Allan et al. (2001b, Figs 6 and 7), even under circumstances of seasonally complex source types and a single seasonal OH sink in source-rich regions (Fig. 1).

The circumstance in which a seasonal source counteracts a seasonal sink to leave an aseasonal $C(t) = C_0$ (viz. $\theta_S = 0$, $S_1/S_0 = \lambda_1/\lambda_0$) also leads to an aseasonal $\delta_C(t) = \delta_0$.

Figure 2(c) illustrates $\delta_C(t)$, using the parameters of Table 1. As for $C(t)$, $\delta_C(t)$ is computed by numerically solving (5) and (6) and (14) with 150-yr spin-up time, yielding a result that is surprisingly well simulated by the sinusoid (15) with (18) and (19). Parameters of that sinusoid are shown in Table 1.

4.3. Phase diagrams

The phase diagrams of Allan et al. (2001b; 2005), when plotted for an individual source type as per Fig. 1, would be represented by a plot of $x = (C(t) - C_0)/C_0$ versus $y = \delta_C(t) - \delta_0$. With the single-harmonic approximations of (7) and (15)

$$x = (C_1/C_0)\cos(\omega t + \theta_C)$$

$$y = \delta_1 \cos(\omega t + \theta_\delta). \tag{21}$$

The sinusoidal parametric equations (21) describe a tilted elliptical shape in (x, y) space as t progresses through an annual period. However, it is clear that, due to (20), the elliptical shape collapses to the straight line $y = \nu x$, with slope characteristic of the KIE (viz. ν of eq. 17), exactly as described by Allan et al. (2001b, Appendix). Figure 4(a) shows the phase diagram corresponding to Fig. 2. In finer detail, the phase diagram actually resembles an ellipse of very high eccentricity that is not apparent in Fig. 4, which is a result of $C(t)$ and $\delta_C(t)$ departing slightly from their sinusoidal idealizations of (21). The TM2 simulations of Allan et al. (2001b) would not have distinguished such high eccentricity from linearity in their Figs 6 and 7 (and Fig. 1 herein).

We now extend our analysis to accommodate multiple seasonal sinks, which Allan et al. (2001b) infer as being responsible for large phase-ellipse tilts based on data from the ETSH atmosphere.

5. Multiple seasonal sinks

The formalism of Section 4 is extended to include multiple seasonal sinks, each with its individual seasonality and KIE. However, to avoid excessive mathematical complexity, we restrict to the case where all sinks are in phase (or in anti-phase). Such a restriction recognizes that all sinks that are strongly seasonal are likely to have their seasonal phase driven to first order by that in solar irradiance, that is, by the seasons themselves. Because it is intended that this formalism should capture the effect of including a highly seasonal, highly fractionating chlorine sink, it could be observed that constructions of this sink are close to being in phase with the principal OH sink (Allan et al., 2001a, 2007).

5.1. Seasonality of total methane

The driving source and multiple sinks take the form

$$S(t) = S_0 + S_1 \cos(\omega t + \theta_S)$$

$$\lambda(t) \equiv \sum_k \lambda_k(t) = \sum_k \{\lambda_{k0} + \lambda_{k1}\cos(\omega t)\} \tag{22}$$

in which λ_{k1} may be negative to accommodate a sink in anti-phase with the primary sink ($k = 1$). It is immediately obvious that multiple in-phase sinks behave exactly like a single sink with summed annual mean and summed amplitude. Consequently, the results of Section 4.1, including (8)–(11), transfer to this case upon replacing λ_0 and λ_1 with Λ_0 and Λ_1 respectively, defined by

$$\Lambda_0 = \sum_k \lambda_{k0}, \quad \Lambda_1 = \sum_k \lambda_{k1}. \tag{23}$$

Thus,

$$S_0 = \Lambda_0 C_0$$

$$C_1 \omega \cos(\theta_C) = S_1 \sin(\theta_S)$$

$$C_1 \omega \sin(\theta_C) = \Lambda_0 C_0 - S_1 \cos(\theta_S). \tag{24}$$

Just as with the single-sink case, $C(t)$ will be aseasonal ($C_1 = 0$) for counteracting source and total sink that are both in

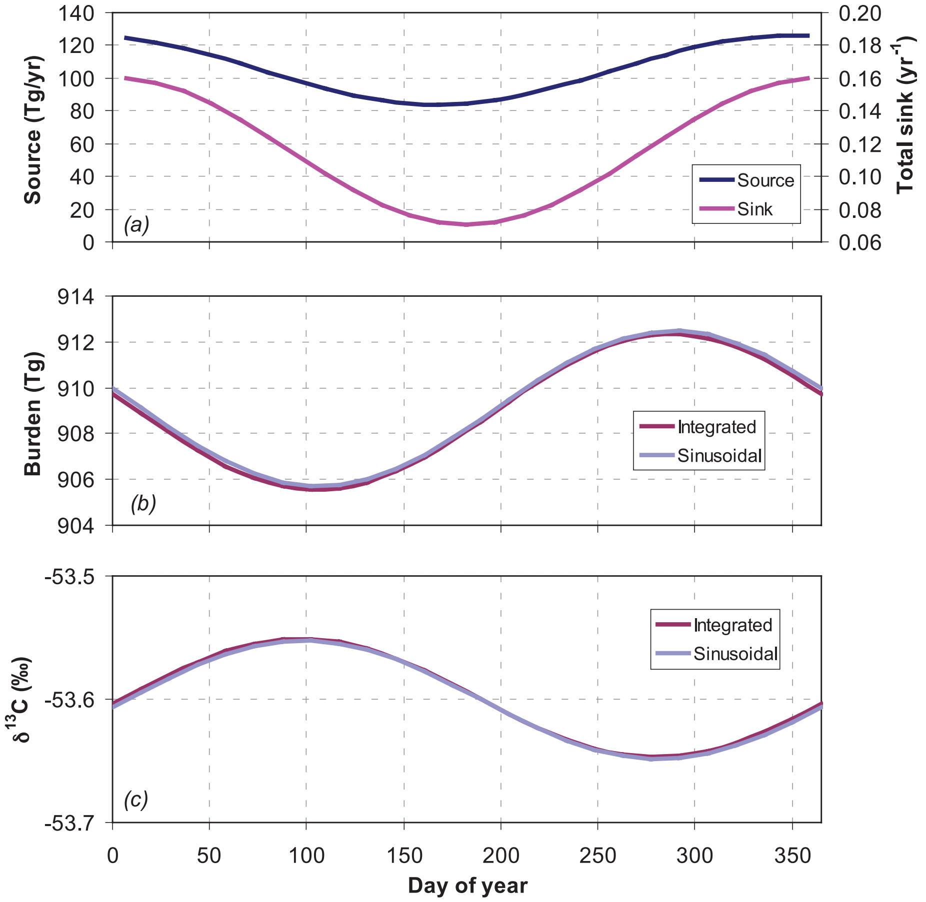

Fig. 3. As for Fig. 2, but for single source and dual sinks using the parameters of Table 1. Panel (a) shows the source and combined sink of eq. (22), and panels (b) and (c) report the counterparts of Fig. 2, but panel (c) has a different scale in δ^{13}C than Fig. 2(c) in light of the much bigger seasonal amplitude.

phase ($\theta_S = 0$) and have identical relative amplitudes ($S_1/S_0 = \Lambda_1/\Lambda_0$).

In the illustrative example of Fig. 3, the highly fractionating, highly seasonal second sink strengthens the combined sink by 5% and also increases its relative seasonal amplitude (Table 1). The source is scaled up (both mean and amplitude) by 5% to restore balance (Fig. 3a). [This approach is analogous to estimating the global source on the basis of top-down budget closure such as is done in IPCC assessments (Denman et al., 2007, Table 7.6)]. The illustration of $C(t)$ in Fig. 3(b) is little different from that in Fig. 2(b) other than its relatively greater seasonal amplitude, and is again little distinguished from the sinusoid (7) with (24) whose parameters are reported in Table 1.

5.2. *Seasonality of* δ^{13}C

The multiple-sink counterpart of (14) for ^{13}CH$_4$ contains the replacement

$$\alpha\lambda(t) \rightarrow \sum_k \alpha_k \lambda_k(t). \tag{25}$$

Here $\alpha_k = 1 + \varepsilon_k$ is the isotope fractionation factor and ε_k is the KIE, for the kth sink.

The counterparts of (16)–(19) can be derived in a similar manner (Appendix C). For this purpose it is useful to define a mean KIE, $\bar{\varepsilon}$, in which ε_k of each sink is weighted by its annual mean

$$\bar{\varepsilon} = \frac{\left(\sum_k \lambda_{k0}\varepsilon_k\right)}{\Lambda_0} \tag{26}$$

together with the corresponding $\bar{\alpha} = 1 + \bar{\varepsilon}$ and $\bar{\nu} \equiv \bar{\varepsilon}(1 + \delta_0)$. The mass-balance counterpart of (18) is

$$\mu = \bar{\nu} \text{ or } \delta_0 = (\delta_S - \bar{\varepsilon})/\bar{\alpha}. \tag{27}$$

Thus, to a good approximation, multiple sink fractionations impose an isotope shift on atmospheric δ^{13}C given by the weighted mean $\bar{\varepsilon}$ of (26), as would be intuitively expected.

However, in balancing seasonality, the counterpart of (19) depends on a mean KIE that is weighted instead by the seasonal amplitudes of the individual sinks (Appendix C) as defined by

$$\tilde{\varepsilon} = \frac{\left(\sum_k \lambda_{k1}\varepsilon_k\right)}{\Lambda_1}. \tag{28}$$

We distinguish $\bar{\varepsilon}$ from $\tilde{\varepsilon}$ by designating them 'mass-balance KIE' and 'seasonal KIE', respectively. With the correspondingly defined $\tilde{\alpha}$ and $\tilde{\nu}$, the counterpart of (19) is

$$\begin{aligned} &\delta_1 \omega C_0 \cos(\theta_\delta) = \mu S_1 \sin(\theta_S) \\ &\delta_1 \omega C_0 \sin(\theta_\delta) = \tilde{\nu}\Lambda_1 C_0 - \mu S_1 \cos(\theta_S). \end{aligned} \tag{29}$$

Contrary to the single-sink situation, the role played by multiple seasonal sinks in isotope mass balance differs from their role in determining atmospheric seasonality: the former is controlled by $\bar{\nu}$ (or $\bar{\varepsilon}$), the latter by $\tilde{\nu}$ (or $\tilde{\varepsilon}$). As a corollary, the seasonal amplitudes of $C(t)$ and $\delta_C(t)$ are no longer as simply related as for the single-seasonal sink case of (20), nor are those seasonalities in strict anti-phase. A result of this is a broadened phase ellipse. The particular circumstance of an aseasonal source is an exception for which

$$\delta_1/|\tilde{\nu}| = C_1/C_0, \quad \theta_C = \pi/2, \quad \theta_\delta = -\pi/2. \tag{30}$$

The single-sink formalism is resurrected when atmospheric seasonality is dominated by source seasonality ($S_1/S_0 \gg \Lambda_1/\Lambda_0$) whereupon the term $\tilde{\nu}\Lambda_1 C_0$ in (29) becomes negligible.

Unexpectedly, the circumstance of counteracting source and sink seasonalities that leads to an aseasonal burden $C(t) = C_0$ (viz. $\theta_S = 0$, $S_1/S_0 = \Lambda_1/\Lambda_0$) no longer leads to an aseasonal $\delta_C(t)$. This is a direct result of $\mu = \bar{\nu}$ being unequal to $\tilde{\nu}$. Conversely, there can be circumstances in which $\delta_C(t)$ but not $C(t)$ becomes aseasonal, namely $\theta_S = 0$ together with

$$\bar{\nu} S_1/S_0 = \tilde{\nu}\Lambda_1/\Lambda_0. \tag{31}$$

These various circumstances can be expected to correspond to unusual phase ellipses with tilts that can be zero [aseasonal $\delta_C(t)$] or infinite [aseasonal $C(t)$].

Figure 3(c) illustrates $\delta_C(t)$ for the dual-sink parameters of Table 1. As with Fig. 2(c), $\delta_C(t)$ is surprisingly little distinguished from its sinusoidal approximation (15) whose parameters are shown in Table 1. However, its seasonal amplitude is enlarged appreciably (by a factor of 4) by the addition of the highly fractionating second sink.

5.3. *Phase diagrams*

Because of the inequality of $\tilde{\nu}$and $\bar{\nu}$, the phase diagram based on (21) does not in general collapse onto a straight line. Figure 4(b) illustrates the elliptically shaped figure based on the parameters of Table 1, and shows also the tilt of that 'ellipse' (using a linear regression line as proxy for the major axis). It is clear that for these parameters the tilt, ν_A, is neither $\tilde{\nu}$ nor $\bar{\nu}$, nor even an intermediate value, so that the inferred 'apparent KIE' given by

$$\varepsilon_A = \nu_A/(1 + \delta_0) \tag{32}$$

is also neither $\tilde{\varepsilon}$ nor $\bar{\varepsilon}$ nor even an intermediate value.

Analytical and numerical exploration suggests that ν_A results from complex interplay between the seasonalities of source and sinks (Appendix D). This implies that not only does ε_A not act as indicator of either $\tilde{\varepsilon}$ or $\bar{\varepsilon}$, but may in fact have a somewhat bizarre value when the circumstances for aseasonal $C(t)$ or $\delta_C(t)$ are nearly met. Figure 5 illustrates this by plotting ε_A calculated from (32), as a function of S_1/S_0 for various choices of phase θ_S, with other dual-sink parameters taken from Table 1. This figure illustrates some non-intuitive features of ε_A that are confirmed by an analytical derivation $\varepsilon_{\text{theor}}$ of ε_A developed in Appendix D: (i) ε_A is independent of δ_S, implying that the δ_S dependence of ν_A is removed by the divisor $(1 + \delta_0)$ in (32); (ii) for an aseasonal source ($S_1/S_0 = 0$), $\varepsilon_A = \tilde{\varepsilon}$ (necessarily independent of θ_S), then is again independent of θ_S at $S_1/S_0 = \Lambda_1/\Lambda_0$ (=0.389 in Fig. 5) where Appendix D confirms its value to be $\frac{1}{2}(\tilde{\varepsilon} + \bar{\varepsilon})$; (iii) for $\theta_S = 0$ (not shown) ε_A becomes singular (infinite slope) at $S_1/S_0 = \Lambda_1/\Lambda_0$ as a result of $C(t)$ becoming aseasonal, which gives rise to a highly non-monotonic function of S_1/S_0 for small θ_S (e.g. for $\theta_S = \pi/24$ in Fig. 5); (iv) ε_A is zero, as a result of aseasonal $\delta_C(t)$, wherever (31) and $S_1 < S_0$ can be simultaneously satisfied, as is demonstrated for $\theta_S = \pi/24$ in Fig. 5.

The high sensitivity of ε_A to values of S_1/S_0 near Λ_1/Λ_0 occurs for only a narrow band of θ_S less than about $\pi/6$ in magnitude, that is for a source out of phase with sinks by less than about 1 month. When these conditions are satisfied, the phase ellipse of Fig. 4(b) becomes much shorter in its extension on the x-axis due to the near-aseasonal $C(t)$. Indeed, as S_1/S_0 approaches and passes through Λ_1/Λ_0, the ellipse turns anti-clockwise (i.e. the tilt approaches the x-axis); as S_1/S_0 further increases it may then turn clockwise. If θ_S is small enough, a positive tilt will be attained for a range of S_1/S_0, as exemplified in Fig. 5, where $\varepsilon_A > 0$ for a range of S_1/S_0 with $\theta_S = \pi/24$.

6. Discussion

We have demonstrated that the imprint of a distributed CH_4 'source type' (fixed $\delta^{13}C$ signature) on a coherent region of the atmosphere exposed to multiple seasonal CH_4 sinks comprises a characteristic seasonal pattern on both atmospheric burden (or mixing ratio) and companion $\delta^{13}C$. For source and sinks that have idealized sinusoidal seasonality, both those seasonal patterns are surprisingly close to sinusoidal. From the seasonal patterns can be constructed phase ellipses as described in Section 2, and the 'apparent KIE', ε_A, of the combined sinks can then be inferred from the 'tilt' of the phase ellipses (slope of the major axis), ν_A, after Allan et al. (2001b, 2005), according to (32). Just how ε_A relates to the KIE in individual sinks depends in a complex way upon the relative strengths and seasonal

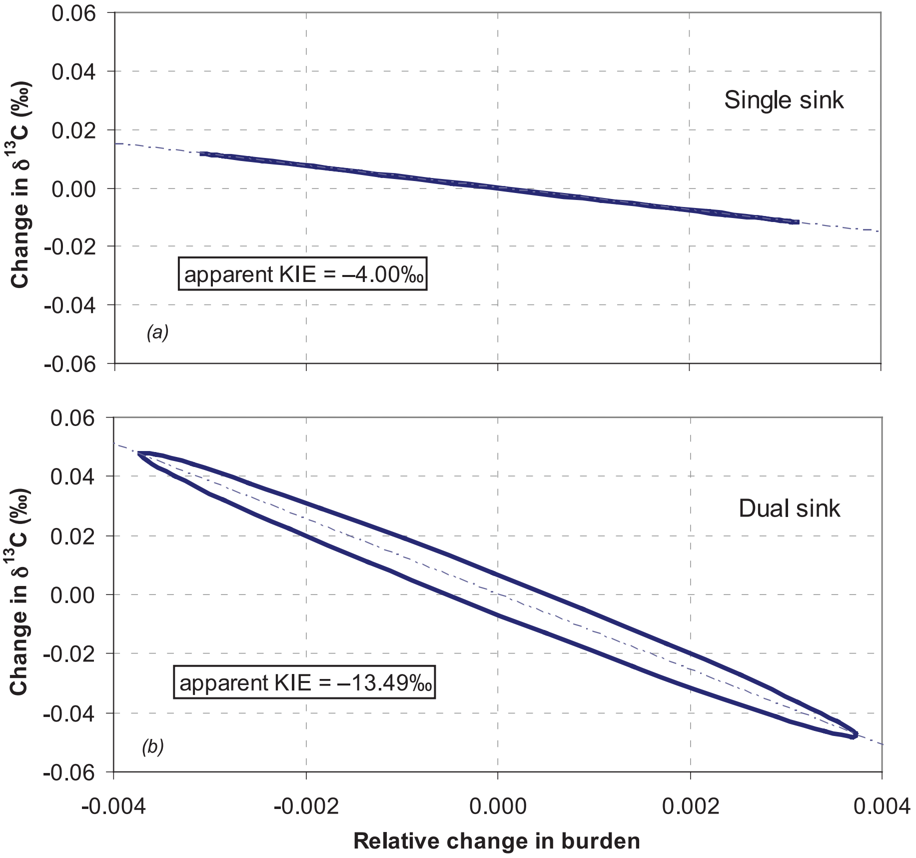

Fig. 4. Phase ellipses based on the simulations of (a) Fig. 2 and (b) Fig. 3. Both panels are on the same scale, and both show the tilted major axis calculated as a regression line of points on the ellipse equally spaced in time (dash–dot line). The 'apparent KIE' values, denoted ε_A in the text and calculated from the major axis slope ν_A as per eq. (32), are reported in each panel. Note that the apparent KIE in panel (b) is larger in magnitude than either $\tilde{\varepsilon}$ or $\bar{\varepsilon}$ in Table 1.

amplitudes of the contributing sinks. Some of these possibilities are as follows:

(i) *Imprint of single seasonal sink.* The seasonalities imprinted on the atmospheric burden and on its companion δ^{13}C are in robust anti-phase, and the ellipse collapses to be indistinguishable from its major axis. The slope of that axis is directly proportional to the KIE of the sink [as per (3) or (32)], regardless of the amplitude and phase of source seasonality. This is illustrated in simulations reported by Allan et al. (2001b) using the 3-D model TM2 with OH as the only seasonal sink and $\varepsilon_{OH} = -5.4‰$. Those simulations with a single source type (called a 'building block' by Allan et al.) featured collapsed ellipses with slopes that recovered $\varepsilon_A = -5.4‰$, irrespective of whether that source type was aseasonal or seasonal (Allan et al., 2001b, Figs 6 and 7; Fig. 1 herein). This does not necessarily mean that aggregated seasonal sources in combination with a single seasonal sink would exhibit collapsed ellipses, for then the isotopic signature of the aggregate source could itself vary seasonally. But aggregated aseasonal sources in combination with a single seasonal sink would exhibit a collapsed ellipse with slope consistent with the sink KIE.

(ii) *Imprint of multiple seasonal sinks in phase, aseasonal source.* A strong anti-phase relationship between imprinted atmospheric burden and δ^{13}C prevails in this case also, with the slope of the collapsed ellipse corresponding to the 'seasonal KIE', $\tilde{\varepsilon}$, defined in (28). The effect of augmenting the major OH sink with a weaker (~5%) atomic chlorine sink that is both highly fractionating ($\varepsilon_{Cl} \approx -62‰$) and more strongly seasonal (Allan et al., 2001a, 2007) is to modify $\tilde{\varepsilon}$ more markedly than the 'mass-balance KIE', $\bar{\varepsilon}$, of (26). Because $\tilde{\varepsilon}$ does not depend on δ^{13}C in the source, δ_S, these same considerations would apply to the combination of multiple seasonal sinks and multiple aseasonal sources.

(iii) *Imprint of multiple seasonal sinks in phase, seasonal source.* As the source seasonal amplitude increases the anti-phase relationship progressively weakens and with it the ellipse eccentricity (e.g. Fig. 4b). The tilt of the ellipse corresponds to a value for ε_A that in the extreme of source-driven seasonality approaches the mass-balance KIE $\bar{\varepsilon}$ of (26), but otherwise can

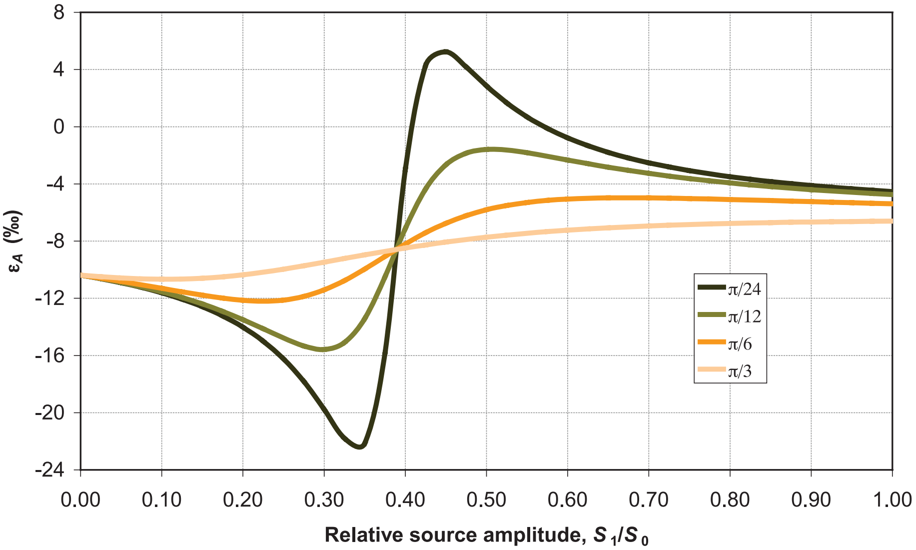

Fig. 5. A plot of ε_{A} versus relative source seasonality, S_1/S_0, with four representative choices of θ_{S} (shown in legend) for the sinusoidal dual-sink model. All parameters except S_1 and θ_{S} are taken from Table 1. For each S_1/S_0, ε_{A} is calculated from the slope ν_{A} of the tilted major axis as per Fig. 4. For $\theta_{\mathrm{S}} > \pi/3$, the plot becomes increasingly flat. Note that all curves pass through the common point where $S_1/S_0 = \Lambda_1/\Lambda_0 = 0.389$. In addition, ε_{A} is an even function of θ_{S} so that negative θ_{S} adds no new information.

vary markedly, even outside the range defined by $\bar{\varepsilon}$ and $\tilde{\varepsilon}$. This unexpected finding arises because ε_{A} is proportional to the ratio of seasonal amplitudes δ_1/C_1, and for multiple sinks C_1 can be unusually small or even vanish while δ_1 remains 'normal' (or vice versa), due to counteracting source and sink seasonalities (Fig. 5, Appendix D).

(iv) *Multiple seasonal sinks, multiple sources.* In general, a phase diagram deduced from aggregated sources may be highly distorted and poorly resembling an ellipse (Allan et al., 2001b). Even for seasonal idealizations such as eq. (6), the 'ellipse' would be broadened and shape-distorted, due in part to multiple seasonal sinks (e.g. Fig. 4b), and in part due to superposed imprints of multiple source types, each with its own seasonality and δ^{13}C signature. Such superposed sources have a seasonally varying δ^{13}C in their aggregate that is not addressed in this paper.

All of the above except (iv) consider individual source types (aseasonal δ_{S}), which are only accessible from model output. When applied to observed mixing ratios and co-located atmospheric δ^{13}C, as well as to model output for the full aggregation of sources, ellipses can be highly distorted with a 'major axis' difficult to isolate (e.g. Allan et al., 2001b, Figs 2 and 3; Allan et al., 2005). This is particularly applicable to sites in source-rich regions such as most NH and tropical sites. It has reduced applicability to remote sites such as in the maritime ETSH (e.g. Allan et al., 2001b, Fig. 1), although not always so (Allan et al., 2005, Fig. 2). This is because of the relative isolation of such ETSH sites (e.g. Baring Head, New Zealand, at 41°S) from source regions and especially from highly seasonal sources, and is the principle reason for the ETSH having regular seasonal patterns of atmospheric mixing ratio (Dlugokencky et al., 1994). Indeed, latitudes south of 30°S are likely to account for only ~2% of global emissions (Fung et al., 1991).

Through examinations of observation-based phase 'ellipses' at Baring Head, Allan et al. (2005, 2007) have argued that air masses in the marine boundary layer at such southern mid-latitudes are affected by atomic chlorine to an extent that can vary markedly from year to year, resulting in elongated shapes that correspond to ε_{A} varying in the range -17 to -6‰ for 1992–2003. Since 2003, ε_{A} appears to have been less variable (Lassey et al., 2010).

However, Fig. 5 raises the possibility that such inter-annual variability could be partly a result of a particular mix of circumstances: if in a particular well-mixed region of the atmosphere an individual source type is nearly in phase with the combined sink (phase difference less than ~1 month) and their relative seasonal amplitudes nearly match, then the corresponding ε_A can be extraordinarily sensitive over an essentially unbounded range to the degree of mismatch in phase and amplitude. This in turn can make that source disproportionately influential in the tilt of the phase ellipse for that region.

As an indicator of a plausible value for S_1/S_0, the relative amplitude in the global CH_4 source is about 0.18, a value based on aggregating all constant and seasonally varying sources described by Allan et al. (2010, Tables 1a and b, Fig. 1). A particular source type within a hemisphere could have a much larger S_1/S_0, with pyrogenic sources from seasonal biomass burning likely to be prominent among these in the SH, even if its seasonality is ~3 months or more out of phase with the sink (Allan et al., 2010, Fig. 1d).

The sources that Baring Head in the ETSH 'sees' would be sources indigenous to the SH plus net 'spillover' sources due to seasonally varying transport between the hemispheres. Lassey et al. (1993) have estimated that annual indigenous and spillover sources are comparable in magnitude. Because air is exchanged between hemispheres on a timescale of order 1 year, Baring Head would likely see spillover sources with much-diminished seasonality despite spillover transport varying seasonally. Thus, relative seasonality of the spillover is likely to be less than 0.18, with consequent ε_A of around -11‰ (Fig. 5), a value which accords well with derivations for the ETSH based on distributions of atomic Cl on which the 'secondary sink' of Table 1 is based (Allan et al., 2007). It is the sources indigenous to the SH that would be seen as the most seasonal at Baring Head, with pyrogenic CH_4 prominent as noted. However, while that source has large seasonality, it is also largely out of phase with the sinks ($|\theta_S| \approx \pi/2$) so that its individual ε_A is insensitive to both seasonality and θ_S (Fig. 5). This probably explains the model result by Allan et al. (2001b, Fig. 5) that varying the pyrogenic source strength affected the eccentricity of the ellipse in the ETSH but had no discernible effect on its tilt.

In a global modelling study with model 'UMeth' (Allan et al., 2007), Allan et al. (2010) examined the sensitivity of ε_A to global source inventory. With OH as the sole seasonal sink having $\varepsilon_{OH} = -3.9$‰, doubling or zeroing individual global source strengths could change the value derived for ε_A at the location of Baring Head only by up to ±1‰ about ε_{OH}. This is consistent with (i) above, in that ε_A would reflect the KIE of the single sink involved. Allan et al. concluded that a highly fractionating second seasonal sink is required to explain the large magnitude of ε_A arising from observations at Baring Head.

That same study (Allan et al., 2010) also explored the two-sink case representing OH and Cl sinks. The same marked adjustments in global source strengths resulted in variations in ε_A also of up to ±1‰ but about a central value of -11‰ (Allan et al., 2010, Table 3). Although that value is fully consistent with Fig. 5 at small S_1/S_0 and/or $|\theta_S| > \pi/3$), and compatible with observation-derived values at Baring Head (Allan et al., 2007), the latter vary interannually by much more than ±1‰. As discussed earlier, such large variations could be partly explained by sensitivity of ε_A to relative source amplitude (S_1/S_0), rather than to source magnitude as investigated by Allan et al. (2010). A more detailed comparison of the analytical results obtained in this paper with the model results of Allan et al. (2010) requires a consideration of seasonal transport and aggregation of seasonal sources that is outside the scope of this paper.

7. Conclusions

We have provided simple analytical support for several empirical features encountered during 3-D modelling of atmospheric CH_4, and insight into their origin. Allan et al. (2001b) found that the atmospheric imprint of a disaggregated source (which they called a 'building block') subjected to a single seasonal sink was a mixing ratio and $\delta^{13}C$ contribution that were always in anti-phase, regardless of the seasonal complexity of that building block. A result of this was a straight-line phase diagram that closely matches the 'KIE line' of eq. (3) with slope proportional to the KIE ε of the particular sink.

The anti-phase property is explained here and shown to be robust, not only when a single seasonal sink is operative with a seasonal source (eq. 20), but also when multiple in-phase seasonal sinks act in concert with an aseasonal source (eq. 30). In the latter case, the KIE predicted by the slope is the 'seasonal KIE' of eq. (28), rather than the sink-weighted KIE of eq. (26) that is implicated in isotope mass balance.

For the case of multiple such sinks acting in concert with a source that varies seasonally, the imprints on mixing ratio and on $\delta^{13}C$ are no longer in anti-phase. This results in a phase diagram that is no longer a straight line, broadening instead into an elliptical shape with reoriented alignment. Unexpectedly, the 'apparent KIE', ε_A, corresponding to that alignment can differ markedly from both the seasonal and mass-balance KIEs, being essentially without bounds when source and sinks are nearly in phase. Appendix D analytically confirms these unexpected features of ε_A, attributing them to counteracting interplays between source and sink seasonalities.

At a particular site in a source-rich region, a phase diagram based either on observation or on output from a 3-D model can bear little relationship to an ellipse (e.g. Allan et al., 2001b, Figs 2 and 3). This can be due to the aggregated effects of multiple seasonal sources, each with its characteristic $\delta^{13}C$ signature, as well as to a succession of different air parcels with trajectories that have experienced different sources. Although CH_4 in the ETSH has more spatial uniformity than north of it (Dlugokencky et al., 1994), such non-elliptical phase diagrams can nevertheless be encountered there too (Allan et al., 2005, Fig. 2). To infer ε_A from such phase diagrams, Allan et al. (2005) applied separate single-harmonic fits to mixing ratio and $\delta^{13}C$ and derived ε_A from the ratio those single-harmonic amplitudes (their eq. 2). For ETSH sites such as Baring Head, New Zealand, such assessed ε_A not only had larger magnitude (~11‰) than OH acting alone would suggest, but that magnitude also exhibited surprisingly high variation from year to year (6–17‰ for 1992–2002). Allan et al. attributed this variation to a variable role of the highly fractionating atomic-chlorine sink. Our analytic derivations reveal unexpected features of ε_A that can include a strongly non-monotonic dependence on source seasonality with the potential to partially explain the observed variability.

Phase ellipses have proven instructive in elucidating the roles of seasonal sinks of atmospheric CH_4. Indeed, without such an approach the role of chlorine in the marine boundary layer of the ETSH would likely not have been uncovered or would have been inferred only qualitatively. There is scope to better understand the determinants of the shapes that emerge in phase diagrams, including the role played by aggregation of multiple isotopically distinct sources, to better elucidate the properties revealed by Allan et al. (2001b, 2005, 2007, 2010).

The formalism developed here has potential application to other long-lived species that are principally removed by OH and with known isotope fractionation. For such species, phase diagrams could be a useful tool for investigating a secondary seasonal sink that has a distinctive fractionation.

8. Acknowledgments

This work was supported by the New Zealand Foundation for Research, Science and Technology under contract C01X0703.

Appendix A: Mass balance for total methane

This appendix outlines the mathematical derivations of eqs (8) and (9) from (5) to (7).

Back-substitution of (6) and (7) into (5) provides the identity (in time):

$$\begin{aligned}-\omega C_1 \sin(\omega t+\theta_C) \equiv{}& S_0+S_1\cos(\omega t+\theta_S)-\{\lambda_0+\lambda_1\cos(\omega t)\}\\ &\times\{C_0+C_1\cos(\omega t+\theta_C)\}.\end{aligned} \tag{A1}$$

Use of standard trigonometric identities provides:

$$\cos(\omega t)\cos(\omega t+\theta_C) = \frac{1}{2}\left\{\cos(\theta_C)+\cos(2\omega t+\theta_C)\right\}. \tag{A2}$$

Upon dropping terms of higher than first harmonic, (A1) can be rewritten as

$$\begin{aligned}&[S_0-\lambda_0 C_0-\frac{1}{2}\lambda_1 C_1\cos(\theta_C)]\\ &\quad\equiv[C_0\lambda_1\cos(\omega t)-S_1\cos(\omega t+\theta_S)+\lambda_0 C_1\cos(\omega t+\theta_C)\\ &\qquad-\omega C_1\sin(\omega t+\theta_C)].\end{aligned} \tag{A3}$$

Identity (A3) is in the form $U\cos(\omega t)+V\sin(\omega t)+W\equiv 0$ in which U, V, W are time independent, and the three functions $\cos(\omega t)$, $\sin(\omega t)$, unity are orthogonal over $0<\omega t<2\pi$. Thus, all of U, V, W can be separately set to zero. The left-hand side (LHS) of (A3) is W which when set to zero immediately leads to (8). The last two terms of the right-hand side (RHS) of (A3) involve cosine and sine of the same angle, and standard trigonometry allows them to be combined into

$$\begin{aligned}&-C_1\sqrt{\omega^2+\lambda_0^2}\sin(\omega t+\theta_C-\eta), \quad \text{where } \tan(\eta)=\lambda_0/\omega\\ &\quad=-\omega' C_1\sin(\omega t+\theta_C') \quad \text{where } \omega'=\sqrt{\omega^2+\lambda_0^2},\ \theta_C'=\theta_C-\eta.\end{aligned} \tag{A4}$$

In practice, because $\eta\approx\lambda_0/\omega\approx 0.02$, θ_C' cannot be distinguished from θ_C, nor ω' from ω, with the result that the combination (A4) effectively reduces to just the last term in (A3). Equated to zero, RHS (A3) then becomes the identity:

$$\omega C_1\sin(\omega t+\theta_C)\equiv C_0\lambda_1\cos(\omega t)-S_1\cos(\omega t+\theta_S). \tag{A5}$$

On expanding the cosine and sine functions in (A5) the coefficients U and V of the orthogonal $\cos(\omega t)$ and $\sin(\omega t)$ can be separately set to zero. The resulting expressions are just eqs (9). Equivalently, eqs (9) follow from setting ωt to 0 and $\pi/2$ in (A5).

Equations (9) can be 'solved' for C_1 and θ_C, although the 'solution' is usually less useful than (9) themselves. By squaring and adding the two eqs (9), θ_C is eliminated to result in

$$(C_1\omega)^2=(\lambda_1 C_0)^2-2\lambda_1 C_0 S_1\cos(\theta_S)+S_1^2. \tag{A6}$$

The phase angle θ_C is determined from the ratio of the two eqs (9):

$$\tan(\theta_C)=(\lambda_1 C_0/S_1)\operatorname{cosec}(\theta_S)-\cot(\theta_S) \tag{A7}$$

subject to $\cos(\theta_C)$ having the same sign as $\sin(\theta_S)$.

Appendix B: Mass balance for stable isotope, single sink

This appendix outlines the mathematical derivations of eqs (18) and (19) from (5) to (7), (14) and (15).

Expand the LHS (14) to yield (omitting for brevity the denotation of explicit time dependences):

$$C\dot{\delta}_C+(1+\delta_C)\dot{C}=(1+\delta_S)S-\alpha\lambda(1+\delta_C)C \tag{B1}$$

in which the over-dot signifies time derivative. From (B1) subtract a multiple $\alpha(1+\delta_C)$ of eq. (5) to cancel the last term in (B1) yielding

$$C\dot{\delta}_C-\varepsilon(1+\delta_C)\dot{C}=(\delta_S-\varepsilon-\alpha\delta_C)S. \tag{B2}$$

Equations (6), (7) and (15) can be back-substituted into (B2). Some simplicity is afforded by the abbreviations μ and ν of (17), and higher harmonics can be dropped following standard trigonometry that relates products of sine and cosine to sine or cosine differences. Then, proceeding as in Appendix A, orthogonality of $\cos(\omega t)$, $\sin(\omega t)$, unity allows the time-independent terms to be set to zero:

$$(\mu-\nu)S_0=\frac{1}{2}\alpha\delta_1\left\{\omega C_1\sin(\theta_C-\theta_\delta)+S_1\cos(\theta_S-\theta_\delta)\right\}. \tag{B3}$$

The dependence on C_1 and θ_C can be removed by either expanding the sine function in (B3) and substituting (9), or, more simply, by setting $\omega t=-\theta_\delta$ in identity (A5), immediately yielding (16).

The harmonic terms arising from (B2) can be expressed as

$$\begin{aligned}&\delta_1\left\{\omega C_0\sin(\omega t+\theta_\delta)-\alpha S_0\cos(\omega t+\theta_\delta)\right\}\\ &\quad\equiv\nu\omega C_1\sin(\omega t+\theta_C)-(\mu-\nu)S_1\sin(\omega t+\theta_S).\end{aligned} \tag{B4}$$

It follows from using (11) and from arguments analogous to those surrounding (A4) that the second term on the LHS (B4) can be ignored compared to the first. Furthermore, the dependence upon C_1 and θ_C can be removed by substituting (A5) into the first term on RHS (B4), yielding

$$\omega C_0\delta_1 \sin(\omega t + \theta_\delta) \equiv \nu C_0\lambda_1 \cos(\omega t) - \mu S_1 \cos(\omega t + \theta_S) \quad \text{(B5)}$$

from which (19) follow by exploiting the orthogonality of $\cos(\omega t)$ and $\sin(\omega t)$.

'Solutions' to (19) follow analogously to (A6) and (A7).

Appendix C: Mass balance for stable isotope, multiple sinks

This appendix outlines the mathematical derivations of eqs (27) and (29) from (5), (7), (14), (15) and (22). The derivation largely parallels that of Appendix B.

Equation (B1) applies here, except that the last term is more complex:

$$\alpha\lambda(1 + \delta_C)C \rightarrow (1 + \delta_C(t))C(t)\,\{\bar{\alpha}\Lambda_0 + \tilde{\alpha}\Lambda_1 \cos(\omega t)\} \quad \text{(C1)}$$

in which $\bar{\alpha} = 1 + \bar{\varepsilon}$ and $\tilde{\alpha} = 1 + \tilde{\varepsilon}$ with $\bar{\varepsilon}$ and $\tilde{\varepsilon}$ given by (26) and (28), respectively. From (C1) subtract a multiple $\tilde{\alpha}(1 + \delta_C)$ of eq. (5) to cancel the last component of the term in (C1) yielding

$$C\dot{\delta}_C - \tilde{\varepsilon}(1 + \delta_C)\dot{C} = (\delta_S - \tilde{\varepsilon} - \tilde{\alpha}\delta_C)S - (\bar{\varepsilon} - \tilde{\varepsilon})\Lambda_0(1 + \delta_C)C. \quad \text{(C2)}$$

The last term is the new addition relative to the single-sink case, and arises only because of the inequality of $\bar{\varepsilon}$ and $\tilde{\varepsilon}$.

Proceeding as in Appendix B, (7), (15) and (22) are back-substituted into (C2) and higher harmonic terms dropped, enabling the segregation of time-independent and harmonic terms into two separate equations. The time-independent equation, simplified by dropping the negligible 'cross-product' terms such as the RHS of (B3), is

$$(\mu - \tilde{\nu})S_0 = (\bar{\nu} - \tilde{\nu})\Lambda_0 C_0 \quad \text{(C3)}$$

in which $\bar{\nu}$ and $\tilde{\nu}$ are defined analogously to ν of (17). On applying the first of eqs (24), (C3) reproduces (27).

The harmonic terms arising from (C2) can be processed exactly as in Appendix B to yield the following analogue of (B5):

$$\omega C_0\delta_1 \sin(\omega t + \theta_\delta) \equiv \tilde{\nu} C_0\Lambda_1 \cos(\omega t) - \mu S_1 \cos(\omega t + \theta_S) \quad \text{(C4)}$$

from which eqs (29) follow.

Appendix D: Tilt of the 'ellipse'

This appendix outlines an analytical derivation of the major axis slope ('tilt') of the phase ellipse, thereby providing analytical support for Fig. 5. The mathematical formulation is borrowed from the regression of y on x in statistical theory, treating points equally spaced in time around the elliptical perimeter as if they were scattered data. In statistical theory, the y-on-x regression line is formally derived by minimising the sum of squares of y-separations between each data point and that line. As long as the seasonal range of $y(t) = \delta_C(t) - \delta_0$ values (i.e. the magnitude of δ_1) is much smaller than the range of $x(t) = (C(t) - C_0)/C_0$ (i.e. the magnitude of C_1/C_0), the y-on-x regression line will be nearly parallel to the x-axis and should be an excellent proxy for a geometrically centred tilt.

From statistical theory, the regression line of y on x for a data set of $N(x, y)$ pairs has slope p/s_x^2, in which s_x^2 is the variance of all N x values and p is the covariance between the x and y paired values. Our approach here considers a continuum of equally spaced times, so that the sums over N become integrals over time rendering N infinitely large. Thus, s_x^2 and p are evaluated as

$$s_x^2 = (2\pi)^{-1} \int_0^{2\pi} x(t)^2 \mathrm{d}(\omega t)$$

and

$$p = (2\pi)^{-1} \int_0^{2\pi} x(t)y(t)\mathrm{d}(\omega t) \quad \text{(D1)}$$

The zero-centred $x(t)$ and $y(t)$ can be closely approximated by the sinusoidal functions (21), enabling the integrals in (D1) to be easily evaluated, to yield

$$s_x^2 = \frac{1}{2}(C_1/C_0)^2 \quad \text{and} \quad p = \frac{1}{2}(C_1/C_0)\delta_1 \cos(\theta_C - \theta_\delta) \quad \text{(D2)}$$

from which the regressed tilt, p/s_x^2, immediately follows, leading to the 'theoretical' apparent KIE from (32):

$$\varepsilon_{\text{theor}} = (1 + \delta_0)^{-1} \frac{\delta_1}{(C_1/C_0)} \cos(\theta_C - \theta_\delta). \quad \text{(D3)}$$

Although $\varepsilon_{\text{theor}}$ can be calculated from (D3) using values such as in Table 1, this simple analytic form belies the complexities evident in Fig. 5. It is therefore instructive to re-express (D3) in terms of the source–sink drivers. This can be accomplished by expanding the cosine and then using expressions (24) and (29), including the analogue of (A6). It is instructive also to introduce the relative seasonal amplitudes

$$f_S = S_1/S_0 \quad \text{and} \quad f_\Lambda = \Lambda_1/\Lambda_0. \quad \text{(D4)}$$

Some manipulation leads to the following re-expression:

$$\varepsilon_{\text{theor}} = \frac{f_S^2\bar{\varepsilon} - (\bar{\varepsilon} + \tilde{\varepsilon}) f_S f_\Lambda \cos(\theta_S) + f_\Lambda^2 \tilde{\varepsilon}}{f_S^2 - 2 f_S f_\Lambda \cos(\theta_S) + f_\Lambda^2}. \quad \text{(D5)}$$

Numerical experimentation using our sinusoidal model with numerically integrated $C(t)$ and $\delta(t)$ confirms that (D5) closely reproduces the actual regression-based fit to the elliptical tilt for a broad range of parameter values. Thus, in general $\varepsilon_{\text{theor}}$ is a linear combination of $\tilde{\varepsilon}$ and $\bar{\varepsilon}$, being equal to the former for an aseasonal source, $f_S = 0$, and approaching the latter when $f_S \gg f_\Lambda$. Equation (D5) also confirms features discussed in Section 5.3. Specifically, the denominator of (D5) vanishes (due to $C_1 = 0$), leading to a singularity in $\varepsilon_{\text{theor}}$, whenever (and only whenever) $\theta_S = 0$ and $f_S = f_\Lambda$. For cases with $C_1 \approx 0$, the conditions of applicability of y on x regression break down because the tilt, measured by $\varepsilon_{\mathrm{theor}}$, is no longer closely parallel to the *x*-axis and/or the ellipse is no longer highly eccentric.

The particular case $f_{\mathrm{S}} = f_{\Lambda}$ in (D5) leads to the simplification that $\varepsilon_{\mathrm{theor}} = (1/2)(\tilde{\varepsilon} + \bar{\varepsilon})$ for non-zero θ_{S} as Fig. 5 demonstrates numerically [i.e. every curve passes through the point (f_{S}, ε_{A}) = (f_{Λ}, $(1/2)(\tilde{\varepsilon} + \bar{\varepsilon})$)].

For the particular case of $\theta_{\mathrm{S}} = 0$ (i.e. source and sinks are in phase) $\varepsilon_{\mathrm{theor}}$ of (D5) simplifies to (provided $f_{\mathrm{S}} \neq f_{\Lambda}$)

$$\varepsilon_{\mathrm{theor}} = \frac{\bar{\varepsilon} f_S - \tilde{\varepsilon} f_{\Lambda}}{f_S - f_{\Lambda}}, \tag{D6}$$

which not only confirms a singularity at $f_{\mathrm{S}} = f_{\Lambda}$, but also emphasizes that $\varepsilon_{\mathrm{theor}}$ vanishes (due to $\delta_1 = 0$) when $\bar{\varepsilon} f_S = \tilde{\varepsilon} f_{\Lambda}$, which restates (31).

References

Allan, W., Lowe, D. C. and Cainey, J. M. 2001a. Active chlorine in the remote marine boundary layer: modeling anomalous measurements of δ^{13}C in methane. *Geophys. Res. Lett.* **28**, 3239–3242.

Allan, W., Manning, M. R., Lassey, K. R., Lowe, D. C. and Gomez, A. J. 2001b. Modeling the variation of δ^{13}C in atmospheric methane: phase ellipses and the kinetic isotope effect. *Global Biogeochem. Cycles* **15**, 467–481.

Allan, W., Lowe, D. C., Gomez, A. J., Struthers, H. and Brailsford, G. W. 2005. Interannual variation of ^{13}C in tropospheric methane: implications for a possible atomic chlorine sink in the marine boundary layer. *J. Geophys. Res.* **110**, D11306, doi:10.1029/2004JD005650.

Allan, W., Struthers, H. and Lowe, D. C. 2007. Methane carbon isotope effects caused by atomic chlorine in the marine boundary layer: global model results compared with southern hemisphere measurements. *J. Geophys. Res.* **112**, D04306, doi:10.1029/2006JD007369.

Allan, W., Struthers, H., Lowe, D. C. and Mikaloff Fletcher, S. E. 2010. Modeling the effects of methane source changes on the seasonal cycles of methane mixing ratio and δ^{13}C in Southern Hemisphere midlatitudes. *J. Geophys. Res.* **115**, D07301, doi:10.1029/2009JD012924.

Bergamaschi, P., Bräunlich, M., Marik, T. and Brenninkmeijer, C. A. M. 2000. Measurements of the carbon and hydrogen isotopes of atmospheric methane at Izaña, Tenerife: seasonal cycles and synoptic-scale variations. *J. Geophys. Res.* **105**, 14 531–14 546.

Bergamaschi, P., Lowe, D. C., Manning, M. R., Moss, R., Bromley, T. and co-authors. 2001. Transects of atmospheric CO, CH_4, and their isotopic composition across the Pacific: shipboard measurements and validation of inverse models. *J. Geophys. Res.* **106**, 7993–8011.

Cantrell, C. A., Shetter, R. E., McDaniel, A. H., Calvert, J. G., Davidson, J. A. and co-authors. 1990. Carbon kinetic isotope effect in the oxidation of methane by the hydroxyl radical. *J. Geophys. Res.* **95**, 22 455–22 462.

Denman, K. L., Brasseur, G., Chidthaisong, A., Ciais, P., Cox, P. M. and co-authors. 2007. Couplings between changes in the climate system and biogeochemistry. In: *Climate Change 2007: The Physical Science Basis. Contribution of Working Group I to the Fourth Assessment Report of the Intergovernmental Panel on Climate Change* (eds. Solomon, S., Qin, D., Manning, M., Chen, Z., Marquis, M. and co-workers). Cambridge University Press, Cambridge, United Kingdom and New York, NY, USA, 499–587.

Dlugokencky, E. J., Steele, L. P., Lang, P. M. and Masarie, K. A. 1994. The growth rate and distribution of atmospheric methane. *J. Geophys. Res.* **99**, 17021–17043.

Dlugokencky, E. J., Houweling, S., Bruhwiler, L., Masarie, K. A., Lang, P. M. and co-authors. 2003. Atmospheric methane levels off: temporary pause or a new steady-state? *Geophys. Res. Lett.* **30**, 1992, doi:10.1029/2003GL018126.

Dlugokencky, E. J., Bruhwiler, L., White, J. W. C., Emmons, L. K., Novelli, P. C. and co-authors. 2009. Observational constraints on recent increases in the atmospheric CH_4 burden. *Geophys. Res. Lett.* **36**, L18803, doi:10.1029/2009GL039780.

Forster, P., Ramaswamy, V., Artaxo, P., Bernsten, T., Betts, R. and co-authors. 2007. Changes in atmospheric constituents and in radiative forcing. In: *Climate Change 2007: The Physical Science Basis. Contribution of Working Group I to the Fourth Assessment Report of the Intergovernmental Panel on Climate Change* (eds. Solomon, S., Qin, D., Manning, M., Chen, Z., Marquis, M. and co-workers). Cambridge University Press, Cambridge, United Kingdom and New York, NY, USA, 129–234.

Francey, R. J. 1985. Cape Grim isotope measurements—a preliminary assessment. *J. Atmos. Chem.* **3**, 247–260.

Francey, R. J., Manning, M. R., Allison, C. E., Coram, S. A., Etheridge, D. M. and co-authors. 1999. A history of δ^{13}C in atmospheric CH_4 from the Cape Grim Air Archive and Antarctic firn air. *J. Geophys. Res.* **104**, 23 631–23 643.

Fung, I., John, J., Lerner, J., Matthews, E., Prather, M. and co-authors. 1991. Three-dimensional model synthesis of the global methane cycle. *J. Geophys. Res.* **96**, 13 033–13 065.

Gupta, M., Tyler, S. and Cicerone, R. 1996. Modeling atmospheric $\delta^{13}CH_4$ and the causes of recent changes in atmospheric CH_4 amounts. *J. Geophys. Res.* **101**, 22 923–22 932.

Heimann, M. 1995. The global atmospheric tracer model TM2. Tech. Rep. 10, Deutsches Klimarechenzentrum, Hamburg, Germany.

Keeling, C. D., Bacastow, R. B., Carter, A. F., Piper, S. C., Whorf, T. P. and co-authors. 1989. A three-dimensional model of atmospheric CO_2 transport based on observed winds. 1. Analysis of observational data. In: *Aspects of Climate Variability in the Pacific and Western Americas* (ed. Peterson, D. H.). American Geophysical Union, Washington, DC, 165–236.

Lassey, K. R., Lowe, D. C., Brenninkmeijer, C. A. M. and Gomez, A. J. 1993. Atmospheric methane and its carbon isotopes in the southern hemisphere: their time series and an instructive model. *Chemosphere* **26**, 95–109.

Lassey, K. R., Lowe, D. C. and Manning, M. R. 2000. The trend in atmospheric methane δ^{13}C and implications for isotopic constraints on the global methane budget. *Global Biogeochem. Cycles* **14**, 41–49.

Lassey, K. R., Brailsford, G. W., Bromley, A. M., Martin, R. J., Moss, R. C. and co-authors. 2010. Recent changes in methane mixing ratio and its ^{13}C content observed in the southwest Pacific region. *J. Integr. Environ. Sci.* **7**, 109–117.

Lowe, D. C., Allan, W., Manning, M. R., Bromley, A., Brailsford, G. and co-authors. 1999. Shipboard determinations of the distribution of ^{13}C in atmospheric methane in the Pacific. *J. Geophys. Res.* **104**, 26 125–26 135.

Mikaloff Fletcher, S. E., Tans, P. P., Bruhwiler, L. M., Miller, J. B. and Heimann, M. 2004a. CH_4 sources estimated from atmospheric observations of CH_4 and its ^{13}C/^{12}C isotopic ratios. 1. Inverse modeling of source processes. *Global Biogeochem. Cycles* **18**, GB4004, doi:10.1029/2004GB002223.

Mikaloff Fletcher, S. E., Tans, P. P., Bruhwiler, L. M., Miller, J. B. and Heimann, M. 2004b. CH_4 sources estimated from atmospheric observations of CH_4 and its $^{13}C/^{12}C$ isotopic ratios. 2. Inverse modeling of CH_4 fluxes from geographical regions. *Global Biogeochem. Cycles* **18**, GB4005, doi:10.1029/2004GB002224.

Miller, J. B., Mack, K. A., Dissly, R., White, J. W. C., Dlugokencky, E. J. and co-authors. 2002. Development of analytical methods and measurements of $^{13}C/^{12}C$ in atmospheric CH_4 from NOAA Climate Monitoring and Diagnostics Laboratory Global Air Sampling Network. *J. Geophys. Res.* **107**, doi:10.1029/2001JD000630.

Platt, U., Allan, W. and Lowe, D. 2004. Hemispheric average Cl atom concentration from $^{13}C/^{12}C$ ratios in atmospheric methane. *Atmos. Chem. Phys.* **4**, 2393–2399.

Rahn, T., Zhang, H., Wahlen, M. and Blake, G. A. 1998. Stable isotope fractionation during ultraviolet photolysis of N_2O. *Geophys. Res. Lett.* **25**, 4489–4492.

Rigby, M., Prinn, R. G., Fraser, P. J., Simmonds, P. G., Langenfelds, R. L. and co-authors. 2008. Renewed growth of atmospheric methane. *Geophys. Res. Lett.* **35**, L22805, doi:10.1029/2008GL036037.

Saueressig, G., Bergamaschi, P., Crowley, J. N., Fischer, H. and Harris, G. W. 1995. Carbon kinetic isotope effect in the reaction of CH_4 with Cl atoms. *Geophys. Res. Lett.* **22**, 1225–1228.

Saueressig, G., Crowley, J. N., Bergamaschi, P., Brühl, C., Brenninkmeijer, C. A. M. and co-authors. 2001. Carbon 13 and D kinetic isotope effects in the reaction of CH_4 with $O(^1D)$ and OH: new laboratory measurements and their implications for the isotopic composition of stratospheric methane. *J. Geophys. Res.* **106**, 23 127–23 138.

Scott, K. M., Lu, X., Cavanaugh, C. M. and Liu, J. S. 2004. Optimal methods for estimating kinetic isotope effects from different forms of the Rayleigh distillation equation. *Geochim. Cosmochim. Acta* **68**, 433–442.

Tarasova, O. A., Brenninkmeijer, C. A. M., Assonov, S. S., Elansky, N. F., Röckmann, T. and co-authors. 2007. Atmospheric CH_4 along the Trans-Siberian Railroad (TROICA) and river Ob: source identification using stable isotope analysis. *Atmos. Environ.* **40**, 5617–5628.

Tyler, S. C., Rice, A. L. and Ajie, H. O. 2007. Stable isotopes in atmospheric CH_4: implications for seasonal sources and sinks. *J. Geophys. Res.* **112**, D03303, doi:10.1029/2006JD007231.